DOI: 10.002/ ((please add manuscript number))
Full Paper

Enhanced CO_2 conversion to CO by silica supported perovskite oxides at low temperatures

Bryan. J. Hare, Debtanu Maiti, Yolanda A. Daza, Venkat R. Bhethanabotla, and John N. Kuhn**

B. J. Hare, D. Maiti, Y. A. Daza, Prof. V. R. Bhethanabotla, Prof. J. N. Kuhn
Department of Chemical & Biomolecular Engineering
University of South Florida (USF)
Tampa, FL 33620, USA
Email: jnkuhn@usf.edu; bhethana@usf.edu

Abstract

Repurposing of CO_2 to valuable hydrocarbons is crucial for energy security and a balanced carbon cycle. Reverse water gas shift chemical looping (RWGS-CL) is capable of efficient CO_2 to CO conversion at a low temperature of ~600 °C with unprecedented rates using the $La_{0.75}Sr_{0.25}FeO_3$ (LSF) perovskite-type oxide amalgamated with silica. The LSF:SiO_2 composite (25% LSF by mass) promotes a notable extent of oxygen vacancies in the active phase, a key parameter for CO_2 conversion. In each of eight RWGS-CL cycles, CO generation yields of LSF:SiO_2 surpass those of LSF alone by about 200%, producing 2.6 mmol CO g_{LSF}^{-1} at a peak rate of 0.8 mmol CO g_{LSF}^{-1} min^{-1}. This significant improvement is concomitant with a decreased average LSF crystalline size retained at these low thermochemical reaction temperatures. Evidence of this enhancement points to perovskite particle size reduction by silica, lattice strain induced by the support, and curtailed quantities of secondary phases that limit accessibility to active surfaces. In this contribution, an appropriate stable platform for improving earth abundancy in perovskite-based redox materials is demonstrated for industrial-scale low temperature CO_2 thermochemical conversion.

Key Words: CO_2 conversion, heterogeneous catalysis, oxide composites, reverse water gas shift chemical looping, characterization

1. Introduction

Throughout preceding decades, global environmental concerns instigated a major shift of research focus and investment in renewable energy generation. However, the need for fossil fuels remains on the rise due to demand for transportation fuels and electricity, resulting in vast emissions of carbon dioxide, a major greenhouse gas. Carbon capture and storage (CCS) is aimed at mitigating this CO_2 emission problem and promote carbon neutrality. However, annual emissions (~35 GT in 2015) continue to relentlessly outweigh the scale of reutilization (estimated ~35 MT in early 2017).[1] This scenario demands several processes that are capable of converting CO_2 to CO to valuable hydrocarbons.[2] The extreme conditions required for natural CO_2 dissociation, over 2000 °C in vacuum,[3] underscore the need for catalytic reinforcements and more energy-efficient processes. Amongst the proposed techniques, solar thermochemical approach (STC), for instance, is particularly attractive.[4-10] It presents the novelty of harvesting solar energy towards repurposing waste CO_2 emissions to hydrocarbons. Corresponding CO selectivity and CO_2 conversion rates are much higher than those of photocatalytic methodologies which struggle to achieve even 1 μmol g_{cat}^{-1} min^{-1}.[11] However, STC processes are typically accompanied by extreme operation temperatures (≥ 1000 °C),[7-8] thereby limiting implementation due to a narrow range of stable materials. A feasible alternative, reverse water gas shift chemical looping (RWGS-CL), is capable of converting CO_2 to CO at much lower temperatures (450 – 700 °C).

The RWGS-CL process (**Figure 1**) is a 2-step process, previously demonstrated by our group,[12-13] whereby mixed metal oxides such as perovskite oxides (ABO_3) are used for generation of 100% selective CO from CO_2. The first step involves partial reduction of the perovskite oxides to their oxygen deficient forms ($ABO_{3-\delta}$) under exposure to hydrogen. The second step is the platform for converting CO_2 to CO over these oxygen vacant perovskites, allowing the oxides to regain their original stoichiometric forms (ABO_3). This cyclic operation converts CO_2 to CO, which can be

subsequently converted to hydrocarbons via Fischer-Tropsch synthesis. The overall process for producing and using these fuels can be CO_2-neutral to the environmental if solar (or other non-fossil fuel derived energy source) is used for hydrogen generation (i.e., water splitting). Low and moderate temperature thermochemical processes permit higher sun-to-fuel efficiencies compared to current and future technologies, making RWGS-CL appropriate for large-scale implementation.[14-15] Wenzel et al. investigated the solar-to-fuels efficiencies of the isothermal chemical looping process and determined a reactor system with separation may consume up to 54% less energy than the conventional reverse water gas shift reaction.[15] Perovskite oxides are key materials that support and enable this operation due to their consistent and intrinsic stability in both stoichiometric and non-stoichiometric forms.[16-20] Lanthanum- and strontium-based materials have revealed good CO_2 conversion performance in both RWGS-CL and STC processes. $La_{0.75}Sr_{0.25}FeO_3$ (LSF), in particular, has shown great promise in

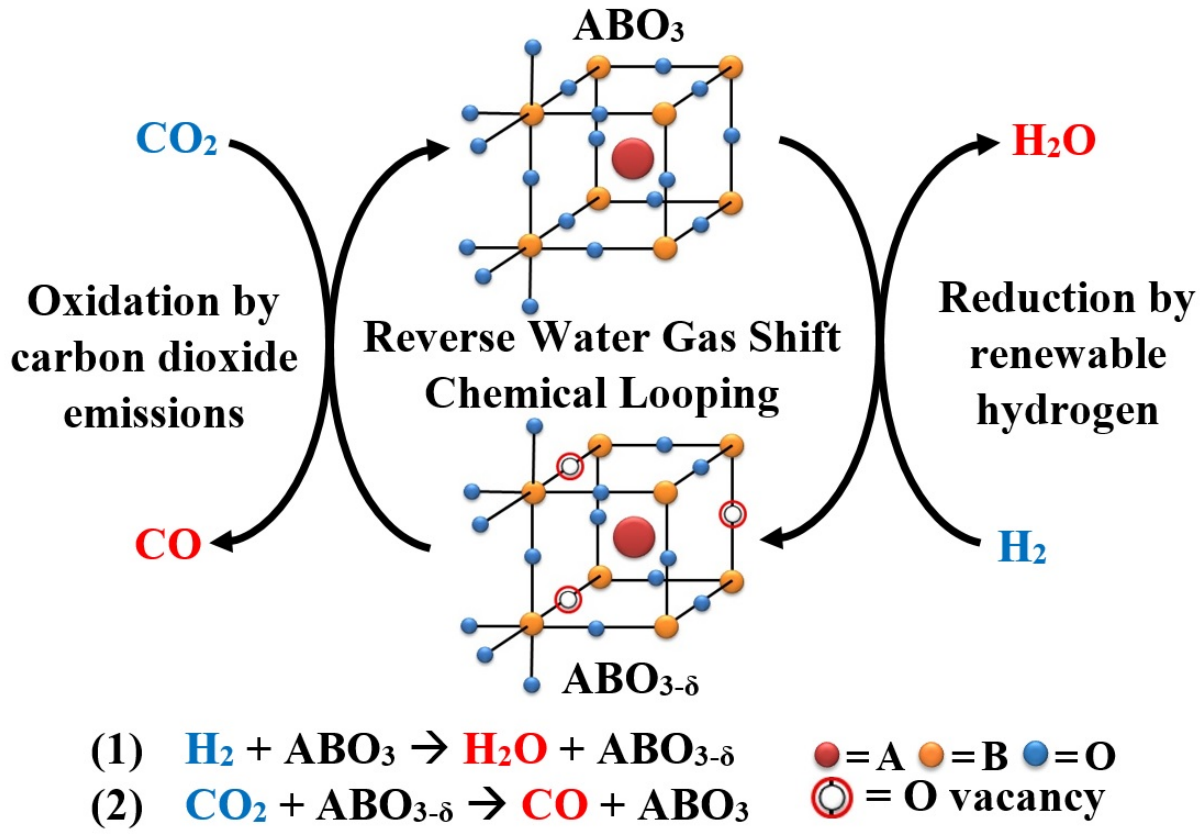

Figure 1: Reverse water gas shift - chemical looping (RWGS-CL) process

RWGS-CL process due to the low energy barrier for oxidation state transitions (Fe^{+3} – Fe^{+2}) during redox cycles.[21] CO_2 also exhibits affinity for the material due to the slight basicity of La,[22] while moderate Sr doping results in slight oxygen deficiency to promote a greater extent of oxygen self-diffusion throughout the lattice.[23] Alternatives such as $LaCoO_3$ demonstrate inadequate structure stability at high reduction temperatures[10, 24] while $LaMnO_3$ exhibits much a higher activation energy for vacancy formation therefore require higher temperatures for redox chemical looping.[25] Our group previously demonstrated indispensable characteristics of LSF such as the perovskite's willingness[26] to retain nonstoichiometry and endure numerous cycles of RWGS-CL at low temperatures.[10] Due to its stability and superior CO_2 conversion rates, LSF is a suitable candidate for RWGS-CL processes.

Modern industrial catalysts in practice are typically structured as pellets, Raschig rings, and other monolithic variations to achieve enhanced surface reactions, minimize pressure drops, promote gas-solid interactions, and prevent activity loss.[27-28] However, mathematical diffusion models suggest an increase in oxide particle radius or membrane thickness severely impedes oxygen self-diffusion and kinetic activity.[29-30] It is thus imperative to investigate the effect of stable supports like silica on the CO_2 conversion performance by these perovskite oxides. Inclusion of oxide supports presents the possibility of expanding the oxygen diffusion network for improved redox reaction performance as shown in other applications.[31-33] Enhanced oxygen self-diffusion, material recyclability, and therefore viability of iron oxides has been demonstrated for chemical looping when supported over titania[34] and perovskite-type oxides.[20, 35] However, supports such as TiO_2 and Al_2O_3 demonstrate strong metal-support interactions which often result in active site encapsulation, even at low temperatures.[36] This would consequentially hinder CO_2 transport to the perovskite surface. Silica, however, is suggested to demonstrate more moderate interactions that are strong enough and suitable for particle segregation yet weak enough to avoid deactivation.[37] The LSF:SiO_2 composite synthesis poses the risk of forming several secondary phases including $FeSiO_3$ and La_2SiO_5 which exhibit unknown consequences to STC

processes[38] due to strenuous attempts at bulk syntheses, many of which have failed.[39] Free energy calculations done by Hubbard and Schlom revealed the spontaneity and readiness of SiO_2 to react at the interface with other unary oxides at elevated temperatures[40] while Kucherov reported transition metal migration through more complex oxides such as zeolites with high Si content.[41] Yet, such atomic volatility contrasts the importance of phase stability delineated by Miller et al. in oxide-impelled syngas production.[42] These conflicting phenomena call for scientists to explore the effect of silica supports on perovskite oxides in regard to their stability and CO_2 conversion performance.

In this study, we combine the LSF perovskite and SiO_2 support into a composite powder as a novel candidate material for efficient CO_2 conversion in RWGS-CL. We also prepare LSF on silicon carbide, a popular non-oxide support[43-44], to test its effect. Different perovskite:silica mass ratios are included, resulting in varying magnitudes of secondary phase formation and surface wetting. Structural stability and long-term activity of top performing materials are demonstrated in 8 cycles of RWGS-CL. We use density functional theory to calculate the oxygen vacancy formation energies of each oxide present in the composite, thus measuring their contribution potentials to redox chemical looping. Crystallographic studies confirm the structural stability of LSF and SiO_2 in recurrent applications and reveal an interfacial wettability effect that reverses sintering of the active phase as confirmed by visual examination through microscopy. Here, we unravel the role of silica in enhancing the CO_2 conversion performance by perovskite-type oxides.

2. Results and Discussion

2.1 Structural characterization

Table 1 consists of each sample synthesized, characterized, and tested with its respective nomenclature. X-ray diffraction (XRD) patterns of $La_{0.75}Sr_{0.25}FeO_3$ (LSF) and SiO_2 along with that of the LSF_{25}/SiO_2 amalgam (25% by weight of LSF) are reported in **Figure 2a**. The composite sample

indicates the dominant presence of pure phase silica (hexagonal quartz [Ref. Code: 00-046-1045]) and LSF phases (orthorhombic structure [Ref. Code: 00-035-1480]). Closer inspection of the 25-40 2θ° (**Figure 2b**) range reveal formation of secondary phases $FeSiO_3$ and La_2SiO_5 in minor amounts. These became more prominent after H_2-reduction and subsequent temperature-programmed oxidation under CO_2 (TPO-CO_2) experiments. The LSF-SiO_2 interface region of the composite material is the most vulnerable to solid state reactions. Yet $FeSiO_3$ and La_2SiO_5 are present as traces and exhibit no adverse effects on the long-term stability of the composite. SiC is used as non-oxygen based reference support to test the effect of Si on stability, secondary phase formation, and CO_2 conversion performance of perovskite:SiC mixtures. The diffraction pattern of the SiC-based amalgam illustrates absence of any secondary phases, even after H_2-reduction and subsequent TPO-CO_2, as is evident from **Figure 2c** and **Figure 2d**.

Table 1: Sample nomenclature for perovskite composites synthesized and tested in temperature programmed experiments. The orthorhombic lattice parameters of LSF in fresh samples are calculated using Ref. Code: 00-035-1480 from the X'Pert Highscore Plus data library. The BET specific surface areas (SSA) are also included for certain samples.

LSF/support (X% w/w)		Sample	LSF orthorhombic lattice parameters of fresh samples (Å)			LSF Cell Volume (Å^3)	$FeSiO_3$ XRD R.I. [a]	La_2SiO_5 XRD R.I. [a]	BET SSA (m^2 g^{-1})
			a	b	c				
None		LSF	5.5107	5.5407	7.7927	237.93	-	-	1.9
Quartz (silica)	25% LSF	LSF_{25}/SiO_2	5.5181	5.5321	7.8137	238.53	1.35 %	0.76 %	1.1 [c]
	50% LSF	LSF_{50}/SiO_2	5.5224	5.5375	7.8263	239.33	1.74 %	0.72 %	-
	75% LSF	LSF_{75}/SiO_2	5.5329	5.5269	7.8254	239.30	0.71 %	0.50 %	-
Black Silicon carbide 70 grit		LSF_{25}/SiC	5.5278	5.5313	7.8223	239.18	n. d. [b]	n. d. [b]	-

[a] *Relative intensities of secondary phase diffraction lines with respect to the dominant crystalline Miller index*

[b] *Nothing detected*

[c] *Quartz SSA (after heat treatment at 950 °C): 1.7 m^2 g^{-1}*

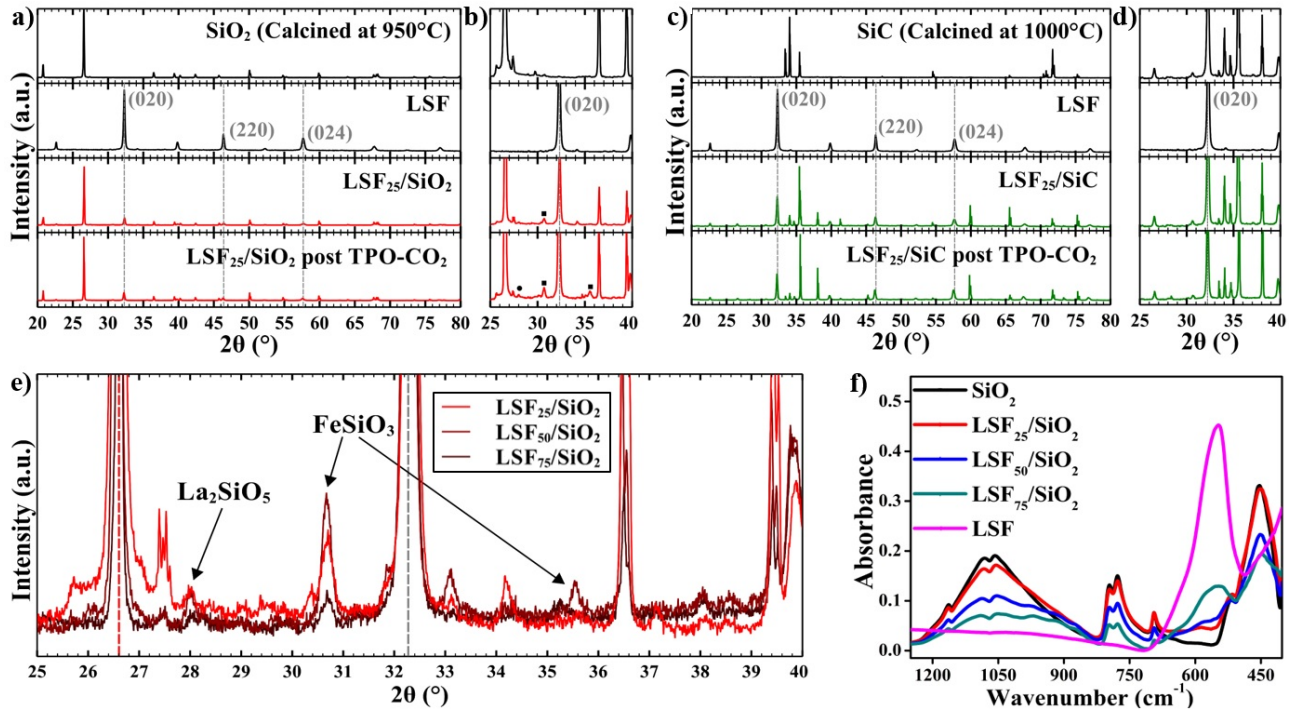

Figure 2: X-ray diffraction and Fourier transform infrared spectroscopy data for LSF-based composites. a) Diffraction patterns of fresh and post TPO-CO_2 LSF_{25}/SiO_2 with constituents and b) closer inspection of 25-40 2θ range to show the emergence of secondary phases. c) Diffraction patterns of fresh and post TPO-CO_2 LSF_{25}/SiC with constituents and d) closer inspection of the aforementioned range to show the absence of secondary phases. e) Diffraction patterns of LSF_X/SiO_2 (X = 25, 50, 75) each show a presence of secondary phases while f) Fourier transform infrared spectra illustrate the consistent decrease in silica content at 1080 cm^{-1} with increasing LSF content.

The presence of secondary phases ($FeSiO_3$ and La_2SiO_5) in the LSF/SiO_2 composites can be consequential to perovskite grain characteristics and CO_2 conversion performance. Therefore, different ratios of LSF and SiO_2 are tested, resulting in varying concentrations of these phases as evident from the relative peak intensities (R.I) at 28.0, 30.6, and 35.5 2θ° (**Figure 2e**). The R.I. of the primary diffraction pattern affiliated with orthorhombic $FeSiO_3$ (Ref. Code: 01-076-0886) changes from 1.35% to 1.74% to 0.71% with increasing LSF content (25% to 75%) as indicated in Table 1. The (-202) XRD

peak of monoclinic La_2SiO_5 (Ref. Code: 00-040-0234) however, remains relatively constant between 0.76% and 0.50% possibly due to high activation energies for La ion migration in perovskites with short O - Fe – O and O – O distances in the lattice.[45] Silica phase transition from quartz to tridymite, a typically lethargic transformation even with alkali promoters,[46] was negligible. Overall, apart from the minor formation of secondary phases, which remain stable over several CO_2 conversion cycles, orthorhombic LSF and hexagonal SiO_2 phases maintain dominancy. Fourier transform infrared spectroscopy (FTIR) results, shown in **Figure 2f**, confirms a consistent trend of decreasing silica peak at 1080 cm^{-1} with increasing LSF in the composites. A notable trend observed in the LSF:SiO_2 amalgams is the change in orthorhombic cell volume with different ratios as reported in Table 1. This pattern is complementary with the formation of secondary phases as shown in Fig 2e. The generation of secondary phases along with surface wetness results in interfacial strain and a slight increase in the cell volume as previously witnessed in interfacial layers between SiO_2 and complex Sr oxides.[47] Calculation of the LSF crystallite size via Scherrer analysis reveals the role of supports in restricting the perovskites from sintering during RWGS-CL experiments as documented in Table 2. This particular role of supports in tuning the LSF crystallite size and strain is fundamental for exploring the underlying mechanism of CO_2 conversion over these composites.

2.2 Temperature-programmed CO_2 conversion experiments

Successful RWGS-CL is contingent on generation of oxygen vacant active sites throughout the perovskite surface and bulk during the reduction step. These active sites are then repurposed for CO_2 to CO conversion in the subsequent oxidation step. Under H_2 flow and increasing temperature, H_2O formation indicates the generation of oxygen vacancies by removal of oxygen installed in the bulk and strongly adsorbed to the surface. Consecutive disintegration of the perovskite phase into simpler, unary and oxides is also observed. These reactions are depicted in **Figure 3a** by H_2O formation (m/z = 18)

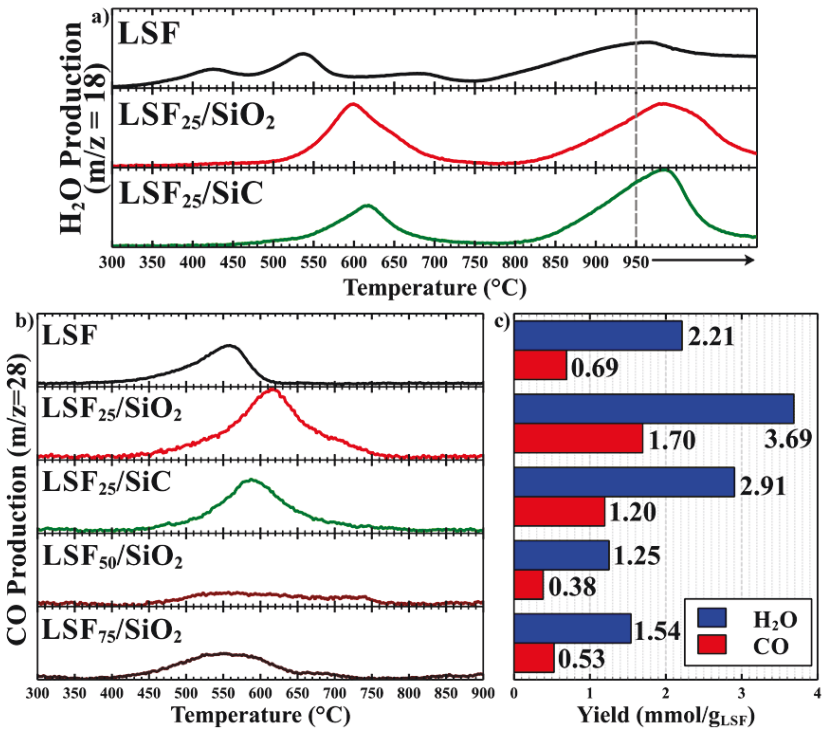

Figure 3: Temperature-programed experimental data with quantifications for H_2O and CO. a) TPR spectrums show 600 °C is an adequate temperature for partial reduction of the materials. b) TPO-CO_2 reveals the changes in CO production with each support and mass ratio. c) H_2O and CO quantifications.

below 700 °C and over 750 °C, respectively. The LSF-based composites exhibit higher peak temperatures, about 600 °C, for H_2O formation than that of LSF (550 °C) alone. This phenomenon may be related to formation of cationic vacancies during the sintering of LSF and SiO_2. A previous study done by Maiti et. al delineated the increase in oxygen vacancy formation energy as the extent of vacancies in the lattice increases.[48] Therefore, the slight but permanent removal of Fe and La from the perovskite lattice results in the formation of $FeSiO_3$ and La_2SiO_5 respectively along with the shift in the perovskite reduction temperature.

Sustainable chemical looping with perovskite oxides requires the formation of oxygen deficient phases without decomposition to disparate species. The TPR profiles suggest 600 °C is an adequate

temperature for achieving numerous vacancies prior to CO_2 conversion while retaining material intactness. CO formation is indicated by the m/z = 28 peak as displayed in **Figure 3b**. Complementary to TPR experiments, CO generates over the LSF composites at about 50 °C higher than over pure LSF. Quantifications in **Figure 3c** shows that H_2O production surpasses that of CO due to a few crucial factors. The entirety of perovskite surface oxygen, for instance, contributes to immense H_2O formation during first-time reduction. Yet replenishment remains highly implausible due to the gradual buildup of kinetic stagnation during CO_2 conversion. Moreover, the activity of oxygen vacant sites towards CO formation is closely related to the net number of oxygen vacancies present at any time. CO_2 adsorption strength over a perovskite oxide increases with the extent of surface oxygen vacancies, reflecting higher probability of conversion.[10] Thus, with progressive refilling of oxygen vacant sites via CO_2 conversion to CO comes a gradual stagnation of surface exchange kinetics resulting in less CO production than that of H_2O in the first cycle.

Capacities of 2.21 mmol H_2O g_{LSF}^{-1} and 0.69 mmol CO g_{LSF}^{-1} are produced during the control experiment with unsupported LSF. While utilization of SiO_2 as a supporting material with 25% LSF results in a 67% increase in H_2O formation capacity at 3.69 mmol g_{LSF}^{-1}, CO production experiences a greater magnitude of improvement of 150% for a total yield of 1.70 mmol g_{LSF}^{-1}. LSF_{25}/SiC also exhibits improved H_2O (2.91 mmol g_{LSF}^{-1}) and CO (1.20 mmol g_{LSF}^{-1}) formation. The XRD patterns of LSF:SiO_2 amalgams after the experiment show the presence of pure orthorhombic LSF and hexagonal SiO_2 phases along with minor concentrations of secondary phases of $FeSiO_3$ and La_2SiO_5. Density functional theory (DFT) based calculations reveal that the LSF phase is the most favorable substrate to accommodate oxygen vacancies while all other phases (SiO_2, $FeSiO_3$ and La_2SiO_5) demand a higher energy input to create oxygen vacancies (**Figure 4a**). CO_2 conversion results for LSF_{25}/SiC validate this hypothesis, for this composite demonstrates enhanced H_2O and CO formation without consisting of SiO_2 or secondary phases. Thus, the reason for better CO_2 conversion is attributed to more surface

area of LSF exposed for gas interactions. This is corroborated by the decreased crystallite size of LSF in the composites compared to its pure phase catalyst.

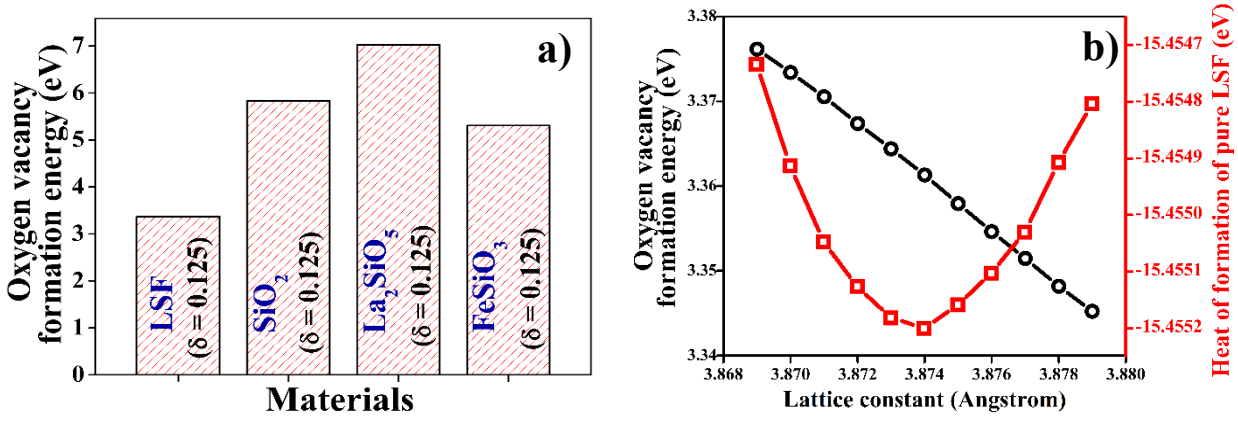

Figure 4: DFT calculations for oxygen vacancy formation. a) Oxygen vacancy formation energies for each oxide species identified in the composite materials. δ represents the extent of oxygen vacancy formation. A value of 0.125 was chosen for consistent comparison. b) Variation of oxygen vacancy formation energy with lattice strain.

Moreover, the increased cell volume of the LSF perovskite indicates the presence of a strained perovskite structure. As shown in **Figure 4b**, an expanded crystal lattice enables oxygen vacancy formation in LSF. Thus, these strained interfaces, suggested by cell volume calculations in **Table 1**, were found to promote oxygen vacancy creation and subsequently enhance CO_2 conversion. SiO_2 shows greater promise than SiC, as it manifests a wettability effect on the perovskite particles. Silica was previously shown to demonstrate affinity for transition metals and is capable of both reducing particle sizes[49] and contact angles.[50] However, there exists an optimum LSF:SiO_2 ratio as is evident from **Figure 3c** whereby LSF_{50}/SiO_2 and LSF_{75}/SiO_2 shows poor CO_2 conversion performance. This is associated with increased formation of $FeSiO_3$ and La_2SiO_5 at the LSF:SiO_2 interface. These secondary phases act as catalyst poisons, reducing the composites' ability to accommodate oxygen vacancies and

CO generation capacity. As aforementioned, they are also believed to be the underlying cause of an increase in E_{vac} due to additional cationic vacancies,[48] and therefore the reduction temperature observed in the TPR experiments. LSF_{25}/SiO_2 however, simultaneously demonstrates minimal secondary phase formation and maximum wettability making the material a suitable candidate for chemical looping.

2.3 Sustained performance in RWGS-CL

The stability and activity of the materials are demonstrated across eight consecutive RWGS-CL cycles (**Figure 5**). LSF_{25}/SiO_2 achieves the highest H_2O and CO yields per perovskite mass basis. By the concluding cycle, the results for LSF_{25}/SiO_2 settle at about 3.10 mmol H_2O g_{LSF}^{-1} per cycle and 2.60 mmol CO g_{LSF}^{-1} per cycle. Overall, LSF_{25}/SiO_2 exhibits 8% and 12% decreases in H_2O and CO production, respectively, after 8 cycles. Unsupported LSF shows no decrease in H_2O production, which stabilizes at about 1.10 mmol H_2O g_{LSF}^{-1}, or CO production, which remain steady around 0.90 mmol CO g_{LSF}^{-1}. LSF_{25}/SiC demonstrates better performance than pure LSF but fell short of LSF_{25}/SiO_2. The extent of oxygen vacancy formation, δ (in $ABO_{3-\delta}$), for LSF is calculated to be 0.26. That of LSF_{25}/SiO_2 and LSF_{25}/SiC are 0.72 and 0.40 respectively. The CO production rate for pure LSF stabilizes over time at 0.93 mmol CO g_{LSF}^{-1} min^{-1} in comparison to 0.80 and 0.38 for LSF_{25}/SiO_2 and LSF/SiC respectively, restrictions potentially imputed to transport limitations exhibited by the supports. Rates are estimated also on an approximated perovskite oxide surface area basis (Table 2). In this metric, the LSF_{25}/SiO_2 composite now surpasses the rate of LSF alone and this is consistent with changes in exposed facets and/or strain that would enhance vacancy formation at the surface.

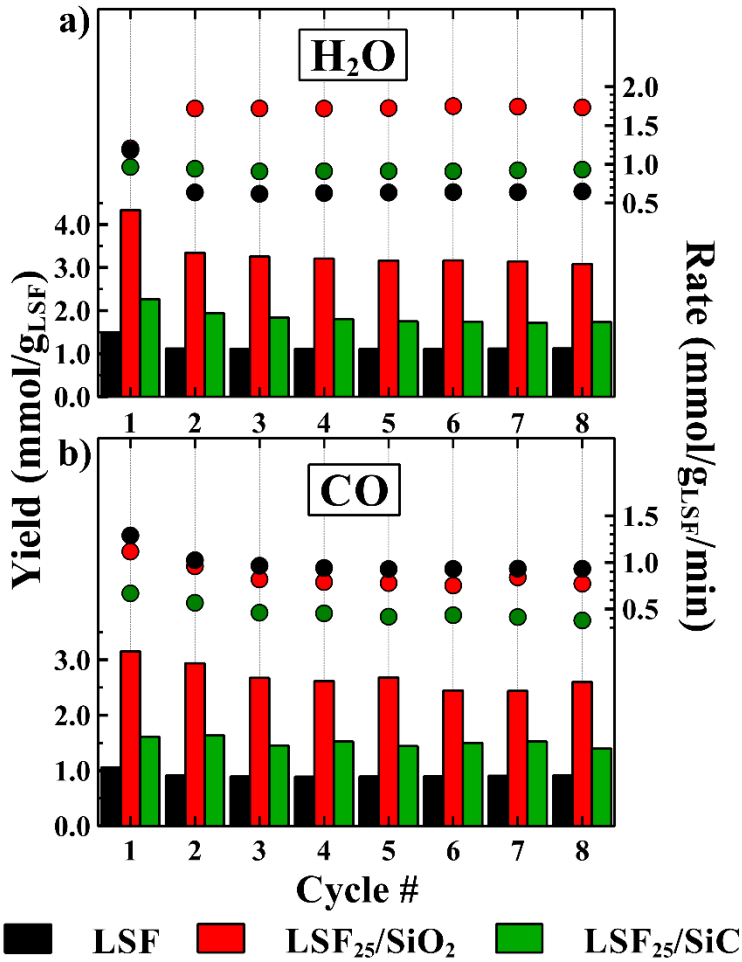

Figure 5: RWGS-CL experiment results for LSF, LSF_{25}/SiO_2, and LSF_{25}/SiC over eight cycles at 600 °C. a) H_2O production yields and peak rates. b) CO production yields and peak rates.

Table 2 – Crystallite size estimations by Scherrer analysis for fresh and post RWGS-CL experiment samples with CO formation rates on the estimated LSF surface area for the final cycle

Sample	Fresh perovskite crystallite size (Å)	Post RWGS-CL perovskite crystallite size (Å)	CO formation rate per LSF surface area (mmol CO $(m^2_{LSF})^{-1}$ min^{-1}) [a]
LSF	350.9	350.9	0.49
LSF_{25}/SiO_2	351.2	269.1	0.64 (0.70 [b])

LSF_{25}/SiC	384.6	336.3	0.18

[a] *Based on LSF surface area when alone and estimated surface area based on changes in crystallite size and proportions of total SSA*

[b] *Estimated on BET SSA (assumes equivalent surface areas per phase)*

Perhaps the greatest significance of the chemical looping data is attributed to the escalation in the H_2O production rate using SiO_2. As aforementioned, accelerated oxygen vacancy formation is concomitant with smaller average perovskite particle radii.[29-30] It is also possible that water spillover to the silica support may enable faster reduction rates, but this effect is anticipated to be minimal in comparison due to the limited water adsorption at these elevated temperatures. Crystallite size reduction, resulting in increased surface area of LSF, is established to be the primary governing criteria for enhanced CO_2 conversion by supported perovskites. Although the average crystallite size of unsupported LSF remains unchanged throughout the 8 cycles, that of the supported samples decreases (Table 2). More in particular, LSF supported on SiO_2 results in a 55% decrease in crystallite size and compliments the loss of bulk oxygen during the course of particle separation. This notable change is illustrated and confirmed by transmission electron microscopy (TEM; **Figure 6)**. While the size of fresh LSF particles, unsupported and supported, remain in the micron threshold, small clusters of LSF nanoparticles formed during RWGS-CL. These nanoparticles are essentially a source of active sites for oxygen vacancy formation and CO_2 conversion. These nanoparticles are not seen to consist of any metallic (Fe, Sr or La) phases nor are they comprised of any binary oxides (Fe oxides, Sr oxides and La oxides). As is evident from figure 6h, the high-resolution image of the nanoparticle structure

reveals the (020) crystal facet that matches that of the fresh samples (figure 6c) and post reaction samples (figure 6e). Strong interaction between LSF nanoparticles and silica rafts restricts their growth and agglomeration, thereby ensuring a surfeit of active sites for CO_2 conversion.

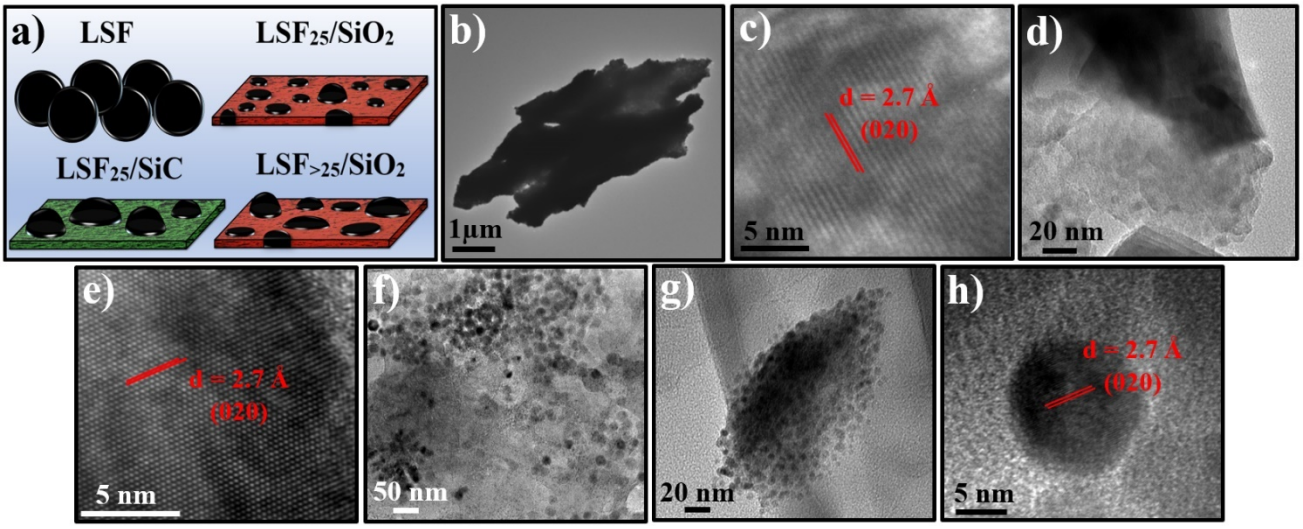

Figure 6: a) Visual schematic of LSF particle size modification by supporting materials during RWGS-CL. TEM images of LSF indicating b) particle size and c) interplanar spacing. Fresh LSF_{25}/SiO_2 d) interface and e) interplanar spacing. LSF_{25}/SiO_2 after 8 RWGS-CL cycles f-h) illustrating a significant decrease in LSF particle size and formation of nanoparticles.

Although silicon carbide demonstrates the same effect according to the Scherrer analysis, it is assured that the particle size reduction magnitude remains much greater when utilizing silica to support perovskite-oxides. Because the black silicon carbide was not reduced, but rather pretreated at 1000 °C in air, there is expected to be a notable presence of oxygen due to a partially oxidized surface[51-52] and iron oxide impurities. Anton et.al concluded that interactions between a support and active phase are much stronger when using a bulk oxide as opposed to an inert support consisting of a few surface oxide layers.[53] Perovskite segregation likely occurred during the second reduction step when surface oxygen was previously removed and the increase in H_2O was noted. The high presence of metallic B-site metals on the perovskite surface during reduction[54-55] is perhaps the driving force for particle size reduction on silica due to the spontaneity of metals to diffuse into the top layers of the oxide bulk. The

kinetic inclination of these ions perhaps pulls apart the large particles to form nanoparticles. This phenomenon is accompanied by the strong surface energy of the reduced perovskite, i.e., oxygen vacant perovskites show strong affinity for species with high oxygen content, such as CO_2 or even potentially SiO_2 regardless of its inert behavior. This surface behavior was not observed in the post TPO-CO_2 samples where CO_2 flows over these samples up to 950 °C. It is thus evident that perovskite particle aggregation is inevitable at high temperatures during synthesis and other STC processes, but may be reversed by subjection to the RWGS-CL process in the presence of appropriate supports at low thermochemical temperatures.

3. Conclusion

This work demonstrated 200% enhancements for CO generation yields for RWGS-CL through the formation of composite materials. SiO_2 is identified as an appropriate supporting material for perovskite-type oxides, $La_{0.75}Sr_{0.25}FeO_3$ (LSF) in this case, due to its wetting influence, ability to reverse LSF particle aggregation resulting from calcination, and induction of lattice strain. Formation inhibiting species (i.e., metal silicate phases, $FeSiO_3$ and La_2SiO_5) that may cause interfacial barriers are restricted by adjusting the perovskite:silica mass ratio and avoiding the high temperatures of other solar thermochemical processes. Long-term stability of the LSF:SiO_2 composite (25 wt% perovskite) is demonstrated over eight cycles of RWGS-CL. Perovskite reduction, the cycle limiting step, is significantly improved to a rate of 1.7 mmol H_2O g_{LSF}^{-1} min^{-1} using the composite while CO generation rates remains stable at 0.8 mmol CO g_{LSF}^{-1} min^{-1}. This study presents a new materials platform towards enhanced reaction activity by oxygen deficient perovskite oxides and provides an avenue to increase earth abundancy of materials used in sustainable production of fuels and chemicals using CO_2 as a feedstock.

4. Experimental Methods

Material Synthesis: A sol gel-based Pechini method was used to synthesize the $La_{0.75}Sr_{0.25}FeO_3$ (LSF) perovskite oxide similar to that proposed by Popa and Kakihana.[56] Using citric acid (CA) (Aldrich >99.5%) as a chelating agent, a 2 M aqueous solution was made with deionized water. Metal precursors $La(NO_3)_3$ (Aldrich 99.9%), $SrCO_3$ (Aesar 99.994%), and $Fe(NO_3)_3$ (Aldrich ACS grade +98%) were each dissolved into the CA solution followed by 2 hr of stirring (200 rpm) at 60°C to minimize mixture variations. Ethylene glycol (EG) (Aldrich >99%) was then added to induce polyesterification as the solution was stirred for 7 hr at 90°C. All reagents were measured to achieve a La : Sr : Fe : CA : EG molar ratio of 0.75 : 0.25 : 1.0 : 10 : 40.[57] The resulting dark red viscous gel was immediately charred at 450°C (25°C/min) for 2 hr. The solidified residue was crushed into powder and further calcined in air at 950°C (25°C/min) for 6 hr to finalize the crystallization of LSF. The perovskite was then combined with silica (quartz, Sigma-Aldrich purum) to obtain a composite material of mass ratios 25%, 50%, and 75% LSF. Black silicon carbide 70 grit (Panadyne Abrasives) was also included as a support and but was first subjected to thermal pretreatment at 1000°C for 2 hr to achieve crystalline phases that would remain stable throughout high-temperature TPO-CO_2 experiments. LSF and the respective materials (X% w/w LSF/support) were grinded together by hand in a mortar and pestle for about 15 min and then heated in air at 950°C for 10 hr to achieve aggregation of constituents.

Temperature-programmed experiments: About 75 mg of each sample was positioned between glass wool within a quartz U-tube. The quartz reactor was then placed within a Thermo Scientific furnace in which the heating ramp was held constant at 10°C/min for all temperature-programmed experiments. The total flow rate was maintained at 50 sccm using Alicat mass flow controllers and consisted of ultra-high purity (UHP) grade gases supplied by Airgas. A MKS Cirrus mass spectrometer (MS) was used to monitor changes in gas flow composition over time. For temperature-programmed reductions (TPR), Gas signals were permitted to stabilize at ambient temperature once the initial flow was

adjusted to 10% H_2 in He (v/v). The temperature was then increased to 950°C (10 °C/min) and held constant until the m/z = 18 signal, representing H_2O, was steady. The TPR profiles revealed a generalized peak reduction temperature for the material set. For temperature-programmed oxidations (TPO-CO_2), each sample was heated under 10% H_2 in He (v/v) flow at 600 °C for 30 min. The oxygen-deficient perovskite material was allowed to cool naturally under He to about 100°C to maintain vacancies. The material was then exposed to a 10% CO_2 in He (v/v) flow and heated to 950°C (10 °C/min) and CO generation was represented by peak formation in the m/z = 28 signal. Quantitative analysis of the resulting data followed procedures previously described.[12]

Structural Characterization: X-ray diffraction was used to probe fresh and post-experimental samples. Main interests included changes in crystalline structure or secondary phases concomitant with solid-state reactions. A Bruker X-Ray Diffractometer with Cu Kα (λ = 0.154 nm) provided patterns at ambient conditions from 20 to 80° (2θ°) with a step size of 0.0102 (2θ°) and 1.2 seconds per step. Raw data and literature patterns from X'Pert Highscore Plus software were juxtaposed for reference when calculating lattice parameters and LSF orthorhombic cell dimensions in each sample as displayed in Table 1. This assay consisted of indexing using Bragg's Law and unique geometrical and interplanar distance equations.[58] Library reference codes are provided when necessary. A Scherrer analysis was also done with a shape factor of 0.9, an acceptable approximation.[58] across the width of the primary LSF (020) diffraction line. This permitted the comparison of crystalline sizes and surface areas of supported and unsupported LSF. FTIR spectroscopy (attenuated total reflectance (ATR)) was performed on all the perovskite-support samples in the Nicolet IS50 instrument from Thermo-Scientific. All the spectra comprised of 50 scans, taken at a resolution of 0.241 cm^{-1} having a data spacing of 0.482 cm^{-1}.

Microscopy: A Tecnai F20 TEM was used for high resolution imaging of LSF particle development after composite synthesis and reaction testing. A Schottky Field emitter sufficed as the electron source

with minimal energy spread (< 0.7 eV) and a point resolution of 0.24 nm. With a line resolution of 0.102 nm, the (020) plane of LSF was probed to calculate the interplanar spacing which remained consistent with crystallographic data.

Physisorption: Specific surface areas were obtained using Quantachrome Autosorb IQ analyzer. After degassing at 300 °C. Adsorption-desorption isotherms were obtained by measuring volume adsorbed by the sample at a set interval of partial pressures (P/P_0) using N_2 as the adsorbate at 77 K. Specific surface area was calculated using Brunauer-Emmet-Teller (BET) method using adsorption data points inside the P/P_0 range of 0.05 to 0.3.

Chemical Looping: LSF_{25}/SiO_2, LSF_{25}/SiC, and unsupported LSF were each tested in eight consecutive isothermal cycles of reverse water gas shift chemical looping (RWGS-CL). Maintaining a total flow rate of 50 sccm throughout the entire experiment, the process began with a 20 min period of 10% H_2 in He (v/v) to reduce the perovskite, thus instigating oxygen vacancy formation. He was flowed again for 20 min before changing the flow to 10% CO_2 in He (v/v) to re-oxidize the perovskite material and generate CO. H_2O and CO production was quantified for each cycle using the same procedures for TPO-CO_2 to test reaction capability and durability over elongated use.

Density-Functional Theory: All the DFT calculations were performed using plane wave basis sets and GGA electron densities using VASP – 5.3.3.[59-63] Projected augmented wave (PAW)[64] potentials were used for treating the core electronic densities. Perdew-Burke-Ernzerhof (PBE) exchange correlation[65] was used. For the study of LSF, a 2×2×2 supercell of 40 atoms (consisting 'n' = 8 unit cells) was used. And hence creating an oxygen vacancy extent (δ) of 0.125 involved removing only one oxygen atom. An average of oxygen vacancy formation energies over different perovskite locations has been reported. A 4×4×4 k-point mesh having Monkhorst Pack grid[66] was generated and was used throughout all calculations over LSF. For other materials like silica, $FeSiO_3$ and La_2SiO_5, k-points were set so as to maintain to a similar k-point grid spacing. Throughout the calculations, an

energy cut off (ENCUT) value of 600 eV was used. In regards to oxygen vacancy formation energy calculations, oxygen over-binding[67] has been accounted for as well. The heat of formation (H_f) of the perovskite oxide was calculated via $H_f = E_{LSF} - \sum_i \mu_i$, where E_{LSF} is LSF's calculated total energy from DFT and μ_i is the ground state fitted elemental reference energy for each of La, Sr, Fe and O.[68] The oxygen vacancy formation energies were calculated as per the equation $E_{vac} = E_{MO_{(x-\delta)}} + \delta \times \frac{n}{2} E_{O_2} - E_{MO_x}$ where, E_{MO_x} is the total energy of the stoichiometric materials (LSF and the metal oxides), n is the number of unit cells in a one supercell, while $E_{MO_{(x-\delta)}}$ is that of the oxygen vacant material and E_{O_2} is the molecular energy of oxygen. The correction factor for oxygen over-binding error (for PBE functionals) by Wang et al.[67] was considered as well.

Acknowledgements

Support from NSF grants CBET-1335817, IIP-1743623, CHE-1531590, and EEC-1560303 and NASA through the Florida Space Grant Consortium is gratefully acknowledged. B.J.H. would like to thank the USF Office of Undergraduate Research and the USF Honors College for financial support. D.M. acknowledges the USF Dissertation Completion Fellowship. Y.A.D. acknowledges the Florida Education Fund for the McKnight Dissertation Fellowship. The authors would like to thank Swetha Ramani and Dr. Yusuf Emirov with assistance with TEM imaging and Adela E. Ramos with assistance with BET analyses. Research Computing, USF is also gratefully acknowledged for the computational resources.

Notes

A provisional patent has been filed by USF on this technology on behalf of the authors.

Author contributions

BJH, YAD, and JNK designed the experiments. BJH performed the majority of the experiments and analyzed the resulting data. DM and VRB designed the simulations. DM performed the simulations and analyzed/modeled the data. BJH and DM drafted the initial manuscript and all authors contributed to writing the revised versions.

References

(1) *The Global Status of CCS: 2016: Summary Report*; Global C.C.S. Institute: 2016; p 28.

(2) Centi, G.; Perathoner, S., *Green carbon dioxide: advances in CO_2 utilization*. John Wiley & Sons: Hoboken, NJ, 2014.

(3) Trevor, J. E.; Kortright, F. L. On chemical equilibria as temperature-functions. *Am. Chem. J.* **1894**, *16*, 611-624.

(4) Ermanoski, I.; Siegel, N. P.; Stechel, E. B. A New Reactor Concept for Efficient Solar-Thermochemical Fuel Poduction. *J. Sol. Energy Eng.* **2013**, *135*.

(5) Furler, P.; Scheffe, J. R.; Gorbar, M.; Moes, L.; Vogt, U.; Steinfeld, A. Solar thermochemical CO_2 splitting utilizing a reticulated porous ceria redox system. *Energy Fuels* **2012**, *26*, 7051-7059.

(6) Lapp, J.; Davidson, J. H.; Lipiński, W. Efficiency of two-step solar thermochemical non-stoichiometric redox cycles with heat recovery. *Energy* **2012**, *37*, 591-600.

(7) McDaniel, A. H.; Miller, E. C.; Arifin, D.; Ambrosini, A.; Coker, E. N.; O'Hayre, R.; Chueh, W. C.; Tong, J. Sr- and Mn-doped $LaAlO_{3-\sigma}$ for solar thermochemical H_2 and CO production. *Energy Environ. Sci.* **2013**, *6*, 2024-2028.

(8) Bork, A. H.; Kubicek, M.; Struzik, M.; Rupp, J. L. M. Perovskite $La_{0.6}Sr_{0.4}Cr_{1-x}Co_xO_{3-\delta}$ solid solutions for solar-thermochemical fuel production: strategies to lower the operation temperature. *J. Mater. Chem. A* **2015**, *3*, 15546-15557.

(9) Daza, Y. A.; Maiti, D.; Hare, B. J.; Bhethanabotla, V. R.; Kuhn, J. N. More Cu, more problems: Decreased CO_2 conversion ability by Cu-doped $La_{0.75}Sr_{0.25}FeO_3$ perovskite oxides. *Surf. Sci.* **2016**, *648*, 92-99.

(10) Daza, Y. A.; Maiti, D.; Kent, R. A.; Bhethanabotla, V. R.; Kuhn, J. N. Isothermal reverse water gas shift chemical looping on $La_{0.75}Sr_{0.25}Co_{(1-Y)}Fe_YO_3$ perovskite-type oxides. *Catal. Today* **2014**, *258*, 691-698.

(11) Takeda, H.; Koike, K.; Inoue, H.; Ishitani, O. Development of an Efficient Photocatalytic System for CO2 Reduction Using Rhenium(I) Complexes Based on Mechanistic Studies. *J. Am. Chem. Soc.* **2008**, *130*, 2023-2031.

(12) Daza, Y. A.; Kent, R. A.; Yung, M. M.; Kuhn, J. N. Carbon dioxide conversion by reverse water gas shift chemical looping on perovskite-type oxides. *Ind. Eng. Chem. Res.* **2014**, *53*, 5828-5837.

(13) Maiti, D.; Hare, B. J.; Daza, Y. A.; Ramos, A. E.; Kuhn, J. N.; Bhethanabotla, V. R. Earth Abundant Perovskite Oxides for Low Temperature CO_2 Conversion. *Energy Environ. Sci.* **2018**, *DOI: 10.1039/C7EE03383D*.

(14) Mallapragada, D. S.; Singh, N. R.; Curteanu, V.; Agrawal, R. Sun-to-Fuel Assessment of Routes for Fixing CO_2 as Liquid Fuel. *Ind. Eng. Chem. Res.* **2013**, *52*, 5136-5144.

(15) Wenzel, M.; Rihko-Struckmann, L. Thermodynamic Analysis and Optimization of RWGS Processes for Solar Syngas Production from CO_2. *AIChE J.* **2017**, *63*, 15-22.

(16) Peña, M. A.; Fierro, J. L. G. Chemical Structures and Performance of Perovskite Oxides. *Chem. Rev.* **2001**, *101*, 1981-2017.

(17) Fan, L.; Zeng, L.; Luo, S. Chemical-Looping Technology Platform. *AIChE J.* **2015**, *61*, 1-22.

(18) Tiep, N. H.; Ku, Z.; Fan, H. J. Recent Advances in Improving the Stability of Perovskite Solar Cells. *Adv. Energy Mater.* **2016**, *6*.

(19) Neal, L. M.; Shafiefarhood, A.; Li, F. Dynamic Methane Partial Oxidation Using a Fe_2O_3@$La_{0.8}Sr_{0.2}FeO_{3-\delta}$ Core–Shell Redox Catalyst in the Absence of Gaseous Oxygen. *ACS Catal.* **2014**, *4*, 3560-3569.

(20) He, F.; Li, F. Perovskite promoted iron oxide for hybrid water-splitting and syngas generation with exceptional conversion. *Energy Environ. Sci.* **2015**, *8*, 535-539.

(21) ten Elshof, J. E.; Bouwmeester, H. J. M.; Verweij, H. Oxygen transport through $La_{1-x}Sr_xFeO_{3-d}$ membranes II. Permeation in air/CO, CO_2 gradients. *Solid State Ionics* **1996**, *89*, 81-92.

(22) Corberan, V. C.; Tejuca, L. G.; Bell, A. T. Surface reactivity of reduced LaFeO3 as studied by TPD and IR spectroscopies of CO, CO_2, and H_2. *J. Mater. Sci.* **1989**, *24*, 4437.

(23) Ullmann, H.; Trofimenko, N.; Tietz, F.; Stöver, D.; Ahmad-Khanlou, A. Correlation between thermal expansion and oxide ion transport in mixed conducting perovskite-type oxides for SOFC cathodes. *Solid State Ionics* **2000**, *138*, 79-90.

(24) Natile, M. M.; Poletto, F.; Galenda, A.; Glisenti, A.; Montini, T.; De Rogatis, L.; Fornasiero, P. $La_{0.6}Sr_{0.4}Co_{1-y}Fe_yO_{3-\delta}$ Perovskites: Influence of the Co/Fe Atomic Ratio on Properties and Catalytic Activity toward Alcohol Steam-Reforming. *Chem. Mater.* **2008**, *20*, 2314-2327.

(25) Badwal, S. P. S.; Jiang, S. P.; Love, J. G.; Nowotny, J.; Rekas, M.; Vance, E. R. Chemical diffusion in perovskite cathodes of solid oxide fuel cells: the Sr doped $LaMn_{1-x}M_xO_3$ (M=Co, Fe) systems. *Ceram. Int.* **2001**, *27*, 419-429.

(26) Teraoka, Y.; Zhang, H.; Purukawa, S.; Yamazoe, N. Oxygen Permeation Through Perovskite-Type Oxides. *Chem. Lett.* **1985**, *14*, 1743-1746.

(27) Campanati, M.; Fornasari, G.; Vaccari, A. Fundamentals in the preparation of heterogeneous catalysts. *Catal. Today* **2003**, *77*, 299-314.

(28) Gallei, E.; Schwab, E. Development of technical catalysts. *Catal. Today* **1999**, *51*, 535-546.

(29) Crank, J., *The mathematics of diffusion*. 2nd. ed.; Oxford University Press: Oxford, England, 1979.

(30) Bredesen, R.; Mertins, F.; Norby, T. Measurements of surface exchange kinetics and chemical diffusion in dense oxygen selective membranes. *Catal. Today* **2000**, *56*, 315-324.

(31) Jiao, F.; Frei, H. Nanostructured Cobalt Oxide Clusters in Mesoporous Silica as Efficient Oxygen-Evolving Catalysts. *Angew. Chem. Int. Ed.* **2009**, *121*, 1873-1876.

(32) Jiao, F.; Frei, H. Nanostructured manganese oxide clusters supported on mesoporous silica as efficient oxygen-evolving catalysts. *Chem. Commun.* **2010**, *46*, 2920-2922.

(33) Rosen, J.; Hutchings, G. S.; Jiao, F. Ordered Mesoporous Cobalt Oxide as Highly Efficient Oxygen Evolution Catalyst. *J. Am. Chem. Soc.* **2013**, *135*, 4516-4521.

(34) Li, F.; Luo, S.; Sun, Z.; Bao, X.; Fan, L. Role of metal oxide support in redox reactions of iron oxide for chemical looping applications; experiments and density functional theory calculations. *Energy Environ. Sci.* **2011**, *4*, 3661-3667.

(35) Chen, Y.; Galinsky, N.; Wang, Z.; Li, F. Investigation of perovskite supported composite oxide oxides for chemical looping conversion of syngas. *Fuel* **2014**, *134*, 521-530.

(36) Gonçalves, G.; Lenzi, M. K.; Santos, O. A. A.; Jorge, L. M. M. Preparation and characterization of nickel based catalysts on silica, alumina and titania obtained by sol–gel method. *J. Non-Cryst. Solids* **2006**, *352*, 3697-3704.

(37) Min, B. K.; Santra, A. K.; Goodman, D. W. Understanding silica-supported metal catalysts: Pd/silica as a case study. *Catal. Today* **2003**, *85*, 113-124.

(38) Jiang, Q.; Tong, J.; Zhou, G.; Jiang, Z.; Li, Z.; Li, C. Thermochemical CO_2 splitting reaction with supported $La_xA_{1-x}Fe_yB_{1-y}O_3$ (A = Sr, Cr, B = Co, Mn; $0 \leq x, y \leq 1$) perovskite oxides. *Sol. Energy* **2014**, *103*, 425-437.

(39) Lindsley, D. H.; Davis, B. T. C.; MacGregor, I. D. Ferrosilite ($FeSiO_3$): Synthesis at High Pressures and Temperatures. *Science* **1964**, *144*, 73-74.

(40) Hubbard, K. J.; Schlom, D. G. Thermodynamic stability of binary oxides in contact with silicon. *J. Mater. Res.* **1996**, *11*, 2757-2776.

(41) Kucherov, A. V.; Slinkin, A. A. Solid-state reaction as a way to transition metal cation introduction into high-silica zeolites. *J. Mol. Catal.* **1994**, *90*, 323-354.

(42) Miller, J. E.; McDaniel, A. H.; Allendorf, M. D. Considerations in the Design of Materials for Solar-Driven Fuel Production Using Metal-Oxide Thermochemical Cycles. *Adv. Energy Mater.* **2014**, *4*, 1300469:1-19.

(43) Ledoux, M. J.; Pham-Huu, C. Silicon carbide: a novel catalyst support for heterogeneous catalysis. *CATTECH* **2001**, *5*, 226-246.

(44) Ledoux, M. J.; Hantzer, S.; Pham-Huu, C.; Guille, J.; Desaneaux, M.-P. New Synthesis and Uses of High-Specific-Surface SIC as a Catalytic Support that Is Chemically Inert and Has High Thermal Resistance *J. Catal.* **1988**, *114*, 176-185.

(45) Islam, M. S. Ionic transport in ABO_3 perovskite oxides: a computer modelling tour. *J. Mater. Chem.* **2000**, *10*, 1027-1038.

(46) Holmquist, S. B. Conversion of Quartz to Tridymite. *J. Am. Ceram. Soc.* **1961**, *44*, 82-86.

(47) McKee, R. A.; Walker, F. J.; Chisholm, M. F. Crystalline Oxides on Silicon: The First Five Monolayers. *Phys. Rev. Lett.* **1998**, *81*, 3014-3017.

(48) Maiti, D.; Daza, Y. A.; Yung, M. M.; Kuhn, J. N.; Bhethanabotla, V. R. Oxygen vacancy formation characteristics in the bulk and across different surface terminations of $La_{(1-x)}Sr_xFe_{(1-y)}Co_yO_{(3-\delta)}$ perovskite oxides for CO_2 conversion. *J. Mater. Chem. A* **2016**, *4*, 5137-5148.

(49) Kim, B. J.; Lee, J.; Yoo, J. B. Sol-gel derived (La, Sr)CoO_3 thin films on silica glass. *Thin Solid Films* **1999**, *341*, 13-17.

(50) Sangiorgi, R.; Muolo, M. L.; Chatain, D.; Eustathopoulos, N. Wettabiility and Work of Adhesion of Nonreactive Liquid Metals on Silica. *J. Am. Ceram. Soc.* **1988**, *71*, 742-748.

(51) Presser, V.; Nickel, K. G. Silica on Silicon Carbide. *Crit. Rev. Solid State* **2008**, *33*, 1-99.

(52) Jorgensen, P. J.; Wadsworth, M. E.; Cutler, I. B. Oxidation of Silicon Carbide. *J. Am. Ceram. Soc.* **1959**, *42*, 613-616.

(53) Anton, R. Interaction of gold, palladium and Au-Pd alloy deposits with oxidized Si(100) substrates. *Thin Solid Films* **1984**, *120*, 293-311.

(54) Ciambelli, P.; Cimino, S.; Lisi, L.; Faticanti, M.; Minelli, G.; Pettiti, I.; Porta, P. La, Ca, Fe oxide perovskites: preparation, characterization and catalytic properties for methane combustion. *Appl. Catal., B* **2001**, *33*, 193-203.

(55) Nishihata, Y.; Mizuki, J.; Akao, T.; Tanaka, H.; Uenishi, M.; Kimura, M.; Okamoto, T.; Hamada, N. Self-regeneration of a Pd-perovskite catalyst for automotive emissions control. *Nature* **2002**, *418*, 164-167.

(56) Popa, M.; Kakihana, M. Synthesis of lanthanum cobaltite ($LaCoO_3$) by the polymerizable complex route. *Solid State Ionics* **2002**, *151*, 251-257.

(57) Ivanova, S.; Senysshyn, A.; Zhecheva, E.; Tenchev, K.; Nikolov, V.; Stoyanova, R.; Fuess, H. Effect of the synthesis route on the microstructure and the reducibility of $LaCoO_3$. *J. Alloys Compd.* **2009**, *480*, 279-285.

(58) Cullity, B. D., *Elements of X-Ray Diffraction*. Addison-Wesley Publishing Company, Inc.: USA, 1956; Vol. 1.

(59) Hohenberg, P.; Kohn, W. Inhomogeneous Electron Gas. *Phys. Rev.* **1964**, *136*, B864-B871.

(60) Kohn, W.; Sham, L. J. Self-Consistent Equations Including Exchange and Correlation Effects. *Phys. Rev.* **1965**, *140*, A1133-A1138.

(61) Kresse, G.; Furthmüller, J. Efficiency of ab-initio total energy calculations for metals and semiconductors using a plane-wave basis set. *Comp. Mater. Sci.* **1996**, *6*, 15-50.

(62) Kresse, G.; Hafner, J. *Ab initio* molecular dynamics for liquid metals. *Phys. Rev. B.* **1993**, *47*, 558-561.

(63) Kresse, G.; Furthmüller, J. Efficient iterative schemes for *ab initio* total-energy calculations using a plane-wave basis set. *Phys. Rev. B.* **1996**, *54*, 11169-11186.

(64) Kresse, G.; Joubert, D. From ultrasoft pseudopotentials to the projector augmented-wave method. *Phys. Rev. B* **1999**, *59*, 1758-1775.

(65) Perdew, J. P.; Burke, K.; Ernzerhof, M. Generalized Gradient Approximation Made Simple. *Phys. Rev. Lett.* **1996**, *77*, 3865-3868.

(66) Monkhorst, H. J.; Pack, J. D. Special points for Brillouin-zone integrations. *Phys. Rev. B* **1976**, *13*, 5188-5192.

(67) Wang, L.; Maxisch, T.; Ceder, G. Oxidation energies of transition metal oxides within the GGA + U framework. *Phys. Rev. B* **2006**, *73*, 195107.

(68) Stevanović, V.; Lany, S.; Zhang, X.; Zunger, A. Correcting density functional theory for accurate predictions of compound enthalpies of formation: Fitted elemental-phase reference energies. *Phys. Rev. B* **2012**, *85*, 115104.

TOC Graphic

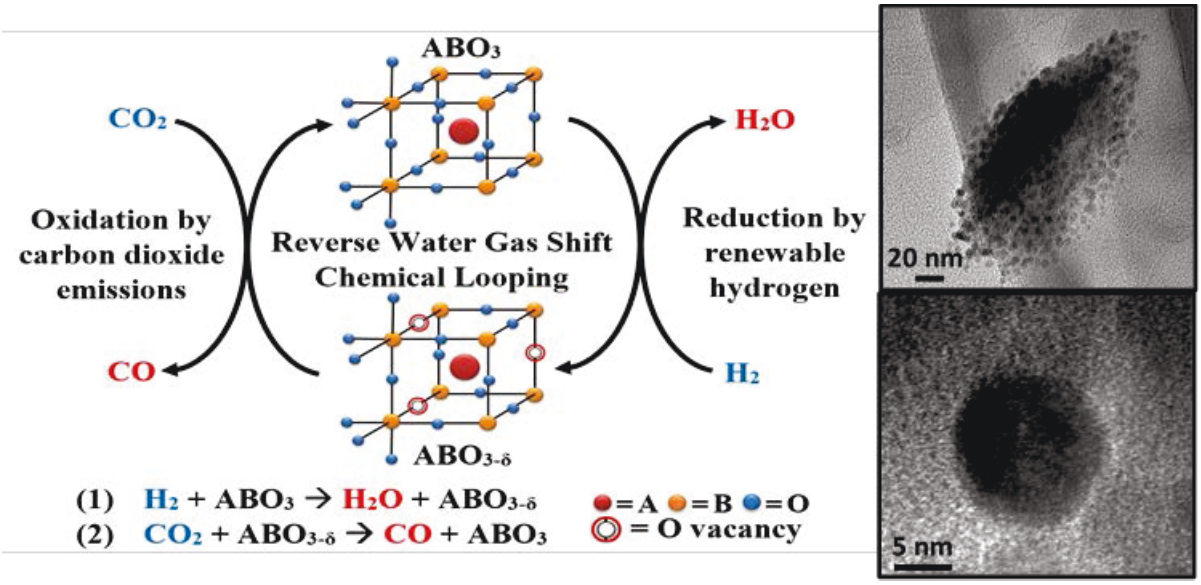
ABO3
CO2
H2O
Oxidation by carbon dioxide emissions
Reverse Water Gas Shift Chemical Looping
Reduction by renewable hydrogen
CO
H2
ABO3-δ
(1) H2 + ABO3 → H2O + ABO3-δ
(2) CO2 + ABO3-δ → CO + ABO3
=A =B =O
= O vacancy
20 nm
5 nm